

## Frequency Domain Two-Stage Beamforming for Phased Array Imaging Using the Fast Hankel Transform

Fool, Fabian; de Wit, Jos; Vos, Rik; Bera, Deep; de Jong, Nico; Verweij, Martin

**DOI**

[10.1109/ULTSYM.2018.8579914](https://doi.org/10.1109/ULTSYM.2018.8579914)

**Publication date**

2018

**Document Version**

Accepted author manuscript

**Published in**

2018 IEEE International Ultrasonics Symposium, IUS 2018

**Citation (APA)**

Fool, F., de Wit, J., Vos, R., Bera, D., de Jong, N., & Verweij, M. (2018). Frequency Domain Two-Stage Beamforming for Phased Array Imaging Using the Fast Hankel Transform. In K. Hashimoto, & C. Ruppel (Eds.), *2018 IEEE International Ultrasonics Symposium, IUS 2018* (Vol. 2018-October). Article 8579914 IEEE. <https://doi.org/10.1109/ULTSYM.2018.8579914>

**Important note**

To cite this publication, please use the final published version (if applicable).  
Please check the document version above.

**Copyright**

Other than for strictly personal use, it is not permitted to download, forward or distribute the text or part of it, without the consent of the author(s) and/or copyright holder(s), unless the work is under an open content license such as Creative Commons.

**Takedown policy**

Please contact us and provide details if you believe this document breaches copyrights.  
We will remove access to the work immediately and investigate your claim.

# Two-Stage Beamforming for Phased Array Imaging using the Fast Hankel Transform

Fabian Fool, *Graduate Student Member, IEEE*, Jos de Wit, Hendrik J. Vos, *Member, IEEE*, Deep Bera, Nico de Jong, *Member, IEEE*, and Martin D. Verweij, *Member, IEEE*

**Abstract**—An ultrasound scan generates a huge amount of data. To form an image this data has to be transferred to the imaging system. This is an issue for applications where the data transfer capacity is limited such as hand-held systems, wireless probes and miniaturized array probes. Two-stage beamforming methods can be used to significantly reduce the data transfer requirements. In the first stage, which is applied in-probe, the amount of data is reduced from channel to scanline data. In the imaging system the data is then beamformed to obtain images that are synthetically focused over the entire image. Currently two approaches exist for the second stage. The first approach is a time-of-flight approach called synthetic aperture sequential beamforming (SASB) that has been developed for both linear and phased arrays. SASB does however introduce artefacts in the image that can be reduced by tapering the first stage scan lines at the cost of lateral resolution. The second approach is based on the wave equation, but a computationally efficient method for phased arrays that is producing sector scan data is lacking. Here we propose an algorithm that uses the fast Hankel transform to obtain a fast algorithm. The imaging performance of this method is evaluated with simulations and experiments. Compared with PSASB, which is an adaption of SASB for phased arrays, our method requires a similar amount of operations to construct the entire image and there is no trade-off between resolution and artefacts. These results show the advantage of using the wave equation instead of a time-of-flight approach.

**Index Terms**—Ultrasound imaging, phased array, synthetic aperture, migration, two-stage beamforming.

## I. INTRODUCTION

AN ultrasound scan generates a huge amount of data. To form an image this data has to be transferred from the probe to the imaging system. For the standard systems found in most hospitals this is not an issue as each element in the probe can be wired out individually. It is an issue for portable hand-held systems, that could for example be used in remote areas, emergency rooms and for use in primary care [1], [2], and probes that are used in size-restricted areas such as Intravascular Ultrasound. As a specific example consider a portable system to be used in remote areas. From a cost

perspective smartphones or tablets would be preferred as imaging system. The probe then has to be able to connect via USB or WiFi to the imaging system. The data transfer requirements for a typical phased array configuration is 1.5 GB/s, assuming 30 frames per second, 128 scanlines per frame, 128 channels per scanline, 2048 samples per trace and 12 bit per sample. While the latest USB standard (3.2 Gen 2x2) would just be able to transfer this amount, the current WiFi standards (802.11ac) cannot. Data reduction is thus required.

A first line of thought might be to construct the image in-probe using Dynamic Receive Focusing (DRF). This would compress the channel data to scanline data. This means that instead of 1.5 GB/s the amount of data would be reduced to 12 MB/s, which is well within the limits of current USB and WiFi standards. In-probe DRF will thus significantly reduce the amount of data. However, the current on-chip DRF solutions [3]–[5] are either too large, have a limited frame rate or a decreased resolution. A method with a reduced in-probe complexity is wanted.

Dynamic receive focusing can be combined with Retrospective Transmit Focusing to improve the lateral resolution [6]. However, depending on its implementation this either implies no data reduction or an even more complex first stage.

Two-stage beamforming is an alternative approach for data reduction [7]–[13]. The first stage consists of a simple single focus Delay-And-Sum (DAS) that reduces the amount of data from channel to scanline data. In the second stage the scanline data is further beamformed in the imaging system to obtain images that are synthetically focused over the entire image. Two-stage beamforming has two main advantages over in-probe DRF. First, the in-probe algorithm has a much lower complexity, allowing for smaller probes and less power dissipation. Second, the lateral resolution is better [7], [8], [13].

Currently there are two approaches available for the second stage: a time-of-flight (TOF) approach based on geometrical path length and an approach based on the wave equation. The first approach is called synthetic aperture sequential beamforming (SASB) and has been developed for linear and phased array imaging [7], [8] the latter called Phased SASB (PSASB). SASB has already been tested in clinical conditions and found to be at least as good as DRF [9], [10]. Furthermore, the feasibility of a wireless ultrasound probe in combination with consumer-level mobile devices that use SASB for beamforming has been demonstrated by Hemmsen *et al.* [11], [12]. A wave equation approach for linear array imaging has been developed by Vos *et al.* [13], based on Stolt migration [14], [15]. The main advantage of this approach over SASB is the

Manuscript received ....; revised .....

The first two authors contributed equally to this work.

F. Fool and J. de Wit are with the with the Laboratory of Acoustical Wavefield Imaging, Department of Imaging Physics, Delft University of Technology, Delft 2628 CJ, The Netherlands. (e-mail: f.fool@tudelft.nl)

D. Bera is with the Biomedical Engineering, Thorax Center, Erasmus MC, University Medical Center Rotterdam, PO BOX 2040, 3000-CA, Rotterdam, the Netherlands.

H. J. Vos, N. de Jong and M. D. Verweij are with the Laboratory of Acoustical Wavefield Imaging, Department of Imaging Physics, Delft University of Technology, Delft 2628 CJ, The Netherlands, and also with the Biomedical Engineering, Thorax Center, Erasmus MC, University Medical Center Rotterdam, PO BOX 2040, 3000-CA, Rotterdam, the Netherlands.

computational efficiency. A better image quality might also be expected because the wave equation is used instead of a TOF approach [16]. However, superior performance in terms of image quality has not been demonstrated with a linear array [13].

A wave equation approach has not yet been developed specifically for the second stage of a two-stage beamforming method for phased array imaging. However, a similar method for a single scanning element on a cylinder does exist [17]. It is possible to adapt this method for phased array imaging, but it is computationally inefficient because one of the integrations cannot be performed using a Fast Fourier Transform (FFT). The latter problem does not arise with Stolt migration used for linear arrays, where after a change of integration variables all integrations can be done using FFTs. Therefore, this specific implementation is not very suitable as a basis for real-time imaging using phased arrays.

In this paper, which is an extension of an earlier proceedings paper, we will develop a computationally efficient two-stage beamforming method for phased array imaging that we will refer to as Phased Array Migration (PAM). The first stage consists of conventional phased array imaging with a single focus in both transmission and reception. The focal points in the first stage can be considered as virtual point sources and point receivers with a limited opening angle doing pulse-echo measurements [7], [8], [13], [18]. The second stage is based on the wave equation in polar coordinates. To make it computationally efficient a change of variables is introduced after which a Fast Hankel Transform (FHT) can be applied. We will show that our method contrary to PSASB has no trade-off between lateral resolution and artefacts, and that the computational performance of our implementation is very similar to PSASB.

This paper is structured as follows. Section II describes the general concept and gives the derivation of the migration and the subsequent implementation. In section III the simulation and experimental setups are described, of which the results are presented in section IV. Section V discusses the developed method and section VI concludes this paper.

## II. CONCEPT AND THEORY

### A. Concept

To use the concept of virtual sources/receivers, the time origin of the first stage scan lines, which are made with a fixed focus in transmit and receive, are shifted according to

$$t' = t - 2\frac{r_f}{c}, \quad (1)$$

in which  $t$  is the original time,  $t'$  is the shifted time,  $r_f$  is the first stage focal depth and  $c$  is the speed of sound in the medium. This time shift splits the dataset in two parts: for  $t' < 0$  the data originates from the pre-focal zone ( $r < r_f$ ) and for  $t' > 0$  the data originates from the the post-focal zone ( $r > r_f$ ). This is also shown in Fig. 1. The shifted data is effectively assumed to originate from a pitch-catch configuration of virtual point sources/receivers located at the focal points.

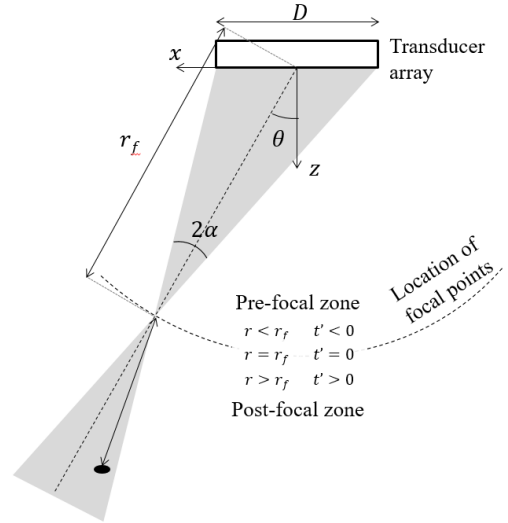


Fig. 1. Schematic overview of the geometry for phased array migration.

The signal that is received from a scatterer by a virtual receiver has travelled through the medium twice: from the source to the reflector and back to the receiver. Since the source and receiver have the same location, these two paths are identical. Hence, the recorded signal is, apart from the amplitude, similar to a signal originating from a transmission at  $t' = 0$  at the scatterer position that has travelled with an effective speed  $\hat{c} = c/2$ . This approach is called the exploding reflector model (ERM) [15]. Every scattering event can be regarded as a sound emission at  $t' = 0$ , that propagates with speed  $\hat{c}$  and which amplitude is proportional to the strength of the scattered signal. The position and strength of the scatterers can be determined by back-propagating the recorded field with speed  $\hat{c}$  to a certain depth and evaluating the field at  $t' = 0$ .

### B. Theory

Stolt migration has been derived in Cartesian coordinates for a linear scan with sources/receivers that are located on a straight line [13]. A detailed derivation of this algorithm is given by Margrave [15]. In a sector scan the virtual sources/receivers are located on a semi-circle that is centred at the transducer midpoint as shown in Fig. 1. Stolt migration is therefore not applicable to this geometry. Hence, we will show the derivation of a similar algorithm for this geometry below.

1) *Phased Array Migration*: The Helmholtz equation in polar coordinates reads [19]

$$r^2 \frac{\partial^2 \tilde{p}}{\partial r^2} + r \frac{\partial \tilde{p}}{\partial r} + \frac{\partial^2 \tilde{p}}{\partial \theta^2} + r^2 k^2 \tilde{p}^2 = 0, \quad (2)$$

in which

$$\begin{aligned} r &= \sqrt{x^2 + z^2} \\ \theta &= \arctan\left(\frac{x}{z}\right), \end{aligned} \quad (3)$$

are the polar coordinates,  $x$  and  $z$  are the Cartesian coordinates,  $\tilde{p}$  is the Fourier transform of the acoustic pressure field

and  $k = 2\pi f/\hat{c}$  is the wavenumber. This equation can be solved by separation of variables, so we write

$$\tilde{p} = R(r)\Theta(\theta), \quad (4)$$

and substitute this in (2) to get

$$\frac{r^2}{R} \frac{\partial^2 R}{\partial r^2} + \frac{r}{R} \frac{\partial R}{\partial r} + \frac{1}{\Theta} \frac{\partial^2 \Theta}{\partial \theta^2} + r^2 k^2 = 0. \quad (5)$$

We can separate this partial differential equation in two ordinary differential equations for  $\Theta$  and  $R$

$$\frac{1}{\Theta} \frac{\partial^2 \Theta}{\partial \theta^2} = -m^2, \quad (6)$$

$$\frac{r^2}{R} \frac{\partial^2 R}{\partial r^2} + \frac{r}{R} \frac{\partial R}{\partial r} + r^2 k^2 - m^2 = 0, \quad (7)$$

where  $m$  is a constant. Equation (6) has the general solution

$$\Theta(\theta) = a_{1,m} e^{-im\theta} + a_{2,m} e^{im\theta}, \quad (8)$$

in which the boundary condition  $\Theta(\theta) = \Theta(\theta + 2\pi)$  makes that  $m$  can only have real integer values.

After introducing the new radial coordinate  $\rho = kr$ , (7) can be rewritten as

$$\frac{\partial^2 R}{\partial \rho^2} + \frac{1}{\rho} \frac{\partial R}{\partial \rho} + R \left(1 - \frac{m^2}{\rho^2}\right) = 0, \quad (9)$$

which is known as Bessel's differential equation [20]. This has the general solution

$$R(\rho) = b_{1,m} H_m^{(1)}(\rho) + b_{2,m} H_m^{(2)}(\rho), \quad (10)$$

where  $H_m^{(1)}$  and  $H_m^{(2)}$  are the  $m^{\text{th}}$  order Hankel functions of the first and second kind. From their asymptotic expansions [20] it follows that  $H_m^{(1)}$  represents a wave that propagates toward the origin and  $H_m^{(2)}$  represents a wave that propagates away from the origin. A general solution to the polar wave equation must contain all possible  $m$ .

To form an image from the measured wavefield at the virtual receivers, first the recorded field has to be transformed to the frequency and angular Fourier domain using the transformation

$$\tilde{p}(r_f, m, f) = \int_{-\infty}^{\infty} \int_0^{2\pi} p(r_f, \theta, t') e^{i(-m\theta + 2\pi f t')} d\theta dt'. \quad (11)$$

Next, the data is propagated to a new depth using the effective speed  $\hat{c} = c/2$ . For the post-focal zone ( $r > r_f$ ) we note that for these depths there are only waves travelling towards the origin that originate from the exploding scatterers. This means that only  $H_m^{(1)}$  is of importance. In view of (10) we can therefore write

$$\tilde{p}(r, m, f) = \tilde{p}(r_f, m, f) \frac{H_m^{(1)}(\hat{k}r)}{H_m^{(1)}(\hat{k}r_f)}, \quad (12)$$

in which  $\hat{k}$  is the wavenumber containing the effective speed  $\hat{c}$ . The final step is to take the inverse Fourier Transform over  $\theta$  and evaluate the field at  $t' = 0$ , which is the time at which

the scatterers exploded in the ERM. The resulting expression is

$$\begin{aligned} p(r, \theta, t' = 0) \\ = \sum_{m=-\infty}^{\infty} \int_{-\infty}^{\infty} \tilde{p}(r_f, m, f) \frac{H_m^{(1)}(\hat{k}r)}{H_m^{(1)}(\hat{k}r_f)} e^{im\theta} df. \end{aligned} \quad (13)$$

This solution is valid for a scatterer in the post-focal zone ( $r > r_f$ ). The solution in the pre-focal zone ( $r < r_f$ ) can be obtained by replacing  $H_m^{(1)}$  by  $H_m^{(2)}$ , as for these depths the waves are travelling away from the origin towards the virtual receivers, and reversing the time axis (i.e.  $t' \rightarrow -t'$ ) before calculating  $\tilde{p}$  using (11).

2) *Fast Hankel Transform*: In its current form (13) cannot be completely evaluated using FFTs only. A similar problem in Cartesian coordinates was solved by Stolt, who changed the integration variables after which all integrations could be evaluated using FFTs [14]. Here there is a ratio of two Hankel functions instead of a complex exponential and therefore exactly the same approach is not possible. However, we can look more closely at the parts in (13) that contain the frequency

$$\bar{p}(r, m) = \int_{-\infty}^{\infty} \frac{\tilde{p}(r_f, m, f)}{H_m^{(1)}(\hat{k}(f)r_f)} H_m^{(1)}(\hat{k}(f)r) df, \quad (14)$$

in which  $\bar{p}$  is the pressure transformed with respect to the angle only. The above equation, which has to be computed separately for each angular frequency, is very similar to a Hankel transform [21]. However, there are two main differences. First of all, the integration is from  $-\infty$  to  $+\infty$  instead of from 0 to  $+\infty$ . A solution is to calculate the integral for positive and negative frequencies separately. A better solution is to drop the integration over the negative frequencies. This is similar to computing the discrete time analytic signal by setting the negative frequencies to zero [22]. This will save computation time in the second stage and because the analytic signal can be used to calculate the envelope of the signal, which is done before image display, it can also save time later in the process. The second difference is that the integration kernel is not a Bessel function of the first kind, but a Hankel function. However, it is still possible to apply the same kind of algorithms. We have applied the same approach as used for the Quasi fast Hankel transform algorithm by Siegman [21]. The basic idea is to introduce the following change of variables

$$\begin{aligned} f &= f_0 e^{+\alpha x}, \\ r &= r_0 e^{-\alpha y}. \end{aligned} \quad (15)$$

This change will turn (14) for the positive frequencies into an equation of the form

$$r_0 e^{-\alpha y} \bar{p}(y, m) = \int_{-\infty}^{\infty} \frac{\bar{p}(x, m)}{H_m^{(1)}(x)} H_m^{(1)}(x - y) dx. \quad (16)$$

Equation (16) has the form of a convolution integral, except that the argument of the rightmost Hankel function is  $x - y$  instead of  $y - x$ . Still, by using the time-reversal property the above equation can be computed using Fourier Transforms as

$$\begin{aligned} r_0 e^{-\alpha y} \bar{p}(y, m) \\ = \mathcal{F}^{-1} \left[ \mathcal{F} \left( \frac{\bar{p}(x, m)}{H_m^{(1)}(x)} \right) \left[ \mathcal{F} \left( H_m^{(1)}(x - y) \right) \right]^* \right]. \end{aligned} \quad (17)$$

The above equation is significantly more computationally efficient than (14) evaluated using a matrix multiplication. However, the requirement of exponentially spaced grids prevent direct application. To solve this nonuniform Fourier Transforms can be used in (17) to apply the algorithm on linearly spaced grids. This approach called the nonuniform fast Hankel transform (NUFHT) has been introduced by Liu and Zhang [23].

3) *Required line density and expected angular frequencies:* The scan line density is an important parameter in the first stage of the imaging process. This parameter determines the density of the virtual point receivers that sample the wavefield and ultimately determines the maximum frame rate. Spatial aliasing can be avoided by choosing the distance between the virtual receivers less than one half of the effective wavelength. This requirement can be described by [13, eq.12]

$$\Delta\theta \leq \frac{\hat{c}}{2r_f f_{\max} \sin \alpha} \quad (18)$$

in which  $\Delta\theta$  is the angle between subsequent ray lines,  $f_{\max}$  the highest frequency in the signal and  $\alpha$  is the half width opening angle that can be geometrically approximated as [8]

$$\alpha \approx \tan^{-1} \left( \frac{D \cos \theta}{2r_f} \right), \quad (19)$$

in which  $D$  is the aperture width and  $\theta$  is the angle of the ray line as shown in Fig. 1.

The required line density gives a limit on the expected angular frequencies. The maximum angular frequency  $m$  for a frequency  $f$  is

$$m_{\max}(f) = \frac{2\pi r_f f \sin \alpha}{\hat{c}}, \quad (20)$$

which can be derived from (18) using

$$m_{\max} = \frac{\pi}{\Delta\theta} \quad (21)$$

and noting that the required spacing is different for each frequency. This limitation on the angular frequency can be used to design a filter that effectively takes into account the limited opening angle of the virtual point sources/receivers. Frequencies that lie outside the maximum expected frequencies are just noise. This filter is due to its form very similar to velocity filters often used in seismic data processing [24].

### C. Implementation

After the single focus scan lines are obtained in the first stage of the imaging process, the second stage beamforming algorithm is applied to the data. The numerical algorithm consists of several subsequent operations:

- 1) Shift the time origin of the image lines to points on a semi-circle with radius  $r_f$ .
- 2) Expand the sector of scanlines to a full circle by zero-padding in the angular direction.
- 3) Transform  $p(r_f, \theta, t')$  to  $\tilde{p}(r_f, m, f)$  by applying a 2D Fast Fourier Transform (FFT).
- 4) Apply a filter to account for the limited opening angle of the virtual sources/receivers.

- 5) Transform  $f$  to  $r$  for each angular frequency  $m$  using the NUFHT.
- 6) Take the Inverse Fast Fourier Transform (IFFT) in the angular direction.
- 7) Discard the ray lines from outside the scanning region.

By using the entire time domain signal in this calculation, and not separating the signals from pre- and post-focal zones, we obtain two important advantages. As the FFT assumes periodic time, circularly connecting the high intensity signal from the focal region to the tapered signal at the domain will result in Gibbs phenomena. Using the entire time signal provides continuity at the boundary between the zones, thereby avoiding Gibbs phenomena that would disturb the final image in the focal region. A second and even greater advantage is that by using the entire time domain signal the far field and the near field region can be reconstructed with the same calculation. Originally, for the calculation of the image in the pre-focal zone the time axis is reversed (i.e.  $t' \rightarrow -t'$ ) before applying the Fourier transform and the Hankel function of the second kind is used instead of the first kind. Instead of reversing the time axis, we can make use of the time reversal property of the Fourier transform and thus replace  $f$  by  $-f$ . By substituting  $f' = -f$  (which implies  $\hat{k}' = -\hat{k}$ ), we get

$$\begin{aligned} \tilde{p}(r_f, m, -f) \frac{H_m^{(2)}(\hat{k}r)}{H_m^{(2)}(\hat{k}r_f)} \\ \rightarrow \tilde{p}(r_f, m, f') \frac{H_m^{(1)}(\hat{k}'r)}{H_m^{(1)}(\hat{k}'r_f)}, \end{aligned} \quad (22)$$

in which we used that  $H_m^{(2)}$  is the complex conjugate of  $H_m^{(1)}$  for real arguments [20, eq. 9.1.40], which results in  $H_m^{(2)}(\hat{k}r_f)$  being equal to  $H_m^{(1)}(-\hat{k}r_f)$ . So the replacement of  $f$  by  $-f$  and the change of the Hankel function mutually cancel and the same expression is used for the far field. Hence, the entire image can be reconstructed with the same calculation.

The expansion to a full circle in step 2 is needed to let the periodic boundary condition in angular direction coincide with the periodicity of the FFT. For this step, it is necessary that  $\Delta\theta = 2\pi/n$  with  $n$  an integer value. Otherwise,  $m$  is no longer an integer value when we perform the Fourier expansion with a FFT.

The filter in step 4 is implemented as a filter with a hard cut-off based on (20) for an unsteered beam (i.e.  $\theta = 0$ ). This means that all  $|m| > m_{\max}(f)$  are set to zero. Usually, this kind of filter produces distortions [25], but there are two reasons why this filter can be used with no problem in our case. First, the maximum angular frequency decreases for higher steering angles and therefore the end of the domain is already slightly tapered. More importantly, due to the use of apodization the effective aperture decreases and therefore also the maximum angular frequency. Due to this the hard cut-off of the filter is already separated from the actual angular frequencies in the signal.

For the nonuniform Fast Fourier Transform (NUFFT) used in step 5 we used the implementation by Fessler and Sutton [26]. This NUFFT uses an upsampled FFT in combination

with a frequency domain interpolation. This particular implementation has a proven low error count [27], [28].

#### D. Comparison with Phased Synthetic Aperture Sequential Beamforming and Dynamic Receive Focusing

We will compare our method with Phased Synthetic Aperture Sequential Beamforming (PSASB) method, an adaption of SASB for phased array imaging. This first stage of PSASB is the same as in our method, but in the second stage the image is beamformed using DAS [7], [8]. The delays for the contributing sources/receivers are calculated from the geometrical path length to the image point. The scan lines that contribute to an image point are selected based on the opening angle. For the comparison we use the implementation for phased array data as used by Bera *et al.* [8]. The contributions of each scan line are weighted using two different windows:

- PSASB 1: a boxcar window, i.e. no weighting of contributing lines.
- PSASB 2: a Hann window, as is done in literature [8].

By using an equal weight for all first stage scan lines in the second stage the lateral resolution will be better as effectively a larger virtual aperture size is used compared to the case where the outer lines have a lower weight. However, the sidelobe level is higher [18], which might appear in the final image as artefacts.

We will also compare our method with Dynamic Receive Focusing (DRF) as SASB is often compared with this method in literature [7], [8].

#### E. Beamwidth and lateral resolution

One of the quality criteria of an ultrasound imaging system is the lateral resolution, which is often defined as the full-width-at-half-maximum (FWHM) or  $-6$  dB width of the pulse-echo point spread function. In most literature, the theoretical beam width is calculated for continuous waves at the centre frequency of the pulse and in the far field approximation. In case broad-band pulses and apodization are used, the PSF width differs significantly from that theoretical value. To correctly account for the broad-band pulse and apodization the far field theoretical beamwidth is determined using the Fraunhofer approximation of the Rayleigh-Sommerfeld integral. A more detailed explanation of how the beamwidth is calculated can be found in the appendix.

### III. METHODS AND MATERIALS

#### A. Experimental setup

Experiments were conducted to investigate the performance of our technique. We used a phased array transducer (ATL P4-1, Phillips Ultrasound, Bothel, Washington, USA) connected to a Verasonics Vantage system (Verasonics Inc., Kirkland, Washington, USA). The system was programmed for a phased array scan with 256 scan lines in a  $90^\circ$  arc, which gives a line density that is more than sufficient according to (18). The received data of each element was filtered using a fourth-order Butterworth bandpass filter with  $-6$  dB cut-off points at

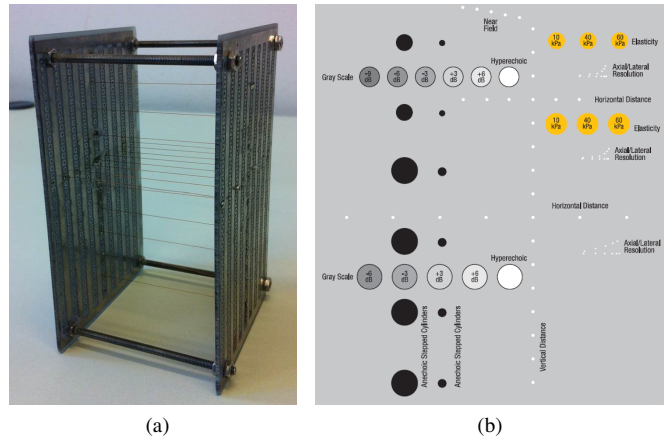


Fig. 2. (a) The phantom with copper wires and (b) the layout of the tissue phantom.

TABLE I  
PARAMETERS USED IN THE EXPERIMENTS.

	Parameter	Value
Transducer	Center frequency	2.5 MHz
	Number of elements	96
	Pitch	295 $\mu\text{m}$
	Element width	245 $\mu\text{m}$
Scan settings	Excitation	1 cycle with equalization
	Apodization	Hamming
	Sampling frequency	10 MHz
	Number of scanlines	256
	Scan angle	$\pm 45^\circ$
	Focal depth	30 mm
Wire phantom	Wire material	Copper
	Wire diameter	120 $\mu\text{m}$
	Medium speed of sound	1487 $\text{m s}^{-1}$
	Medium attenuation	Negligible
Tissue phantom	Model	CIRS 040GSE
	Imaging depth	170 mm
	Medium attenuation	0.5 dB $\text{MHz}^{-1} \text{cm}^{-1}$

1 and 4 MHz, and stored for further processing. This data is used as basis for all imaging methods.

Two different phantoms have been used in the measurements: a phantom with thin copper wires in a water bin and a tissue mimicking phantom. The wire phantom is custom built from two boards with holes, between which thin copper wires with a diameter of 120  $\mu\text{m}$  are attached as line scatterers, as shown in Fig. 2a. The vertical distance between the wires is about 10 mm and the horizontal distance about 8 mm. Other experiments are performed on a commercial tissue mimicking phantom (040-GSE, CIRS, Norfolk, Virginia, USA) with nylon wires and cysts with varying scattering properties. For the measurements on both phantoms, a Hamming window apodization was applied in both transmission and reception for all methods. The experimental settings are summarized in Table I.

For the first stage beamforming a straightforward single focus delay-and-sum (DAS) algorithm was used. In order to avoid discretization errors, the time delays between the elements were applied as phase shifts in the frequency domain

main. The radial grid spacing for the two-stage beamforming methods was chosen to be 1/4 of the wavelength corresponding to the centre frequency, which is the same spacing as used for DRF. For DRF and the second stage of PSASB the data were first upsampled using Matlab's resample function from 10 to 100 MHz to avoid discretization errors. The greyscale images were made by first applying a time gain compensation such that the amplitudes of the central row of scatterers were close to 0 dB. After this the envelope of the time domain signal for each radial image line is calculated. Finally, the amplitude is log compressed and displayed on a Cartesian grid.

### B. Simulations

Simulations have been performed using FieldII [29], [30] only for the wire phantom. To obtain results similar to the measurements, the pulse-echo response of one central element of the probe has been measured and used as excitation pulse in the simulations. The data has been simulated with a sampling rate of 100 MHz, but before further processing the data was downsampled to 10 MHz. After this, the data were processed equally to the measurement data.

### C. Measures of image quality

The quality of the images was evaluated on the basis of the  $-6$  dB lateral PSF width and the contrast-to-noise-ratio (CNR). The lateral PSF width was determined from the vertical row of line scatterers in both phantoms. All data was linearly interpolated in the angular direction before determining the lateral width. The  $-6$  dB lateral width is compared with the width obtained from the Rayleigh-Sommerfeld integral.

The effect of the  $f$ -number on the  $-6$  dB lateral resolution was investigated for  $f$ -numbers between 0.25 and 4. The  $f$ -numbers were varied by changing the focal depth for a constant aperture. Measurements on the wire phantom with apodization were used for this evaluation.

The imaging performance for an anechoic cyst is evaluated using the CNR that is defined as [31]

$$\text{CNR} = \frac{|\mu_s - \mu_c|}{\sqrt{(\sigma_s^2 + \sigma_c^2)}}, \quad (23)$$

in which  $\mu_c$  and  $\mu_s$  are the mean amplitudes in the cyst region and the speckle region before log compression, and  $\sigma_c$  and  $\sigma_s$  are the corresponding variances. These values are calculated for 2 anechoic cylinders of 6.7 mm diameter that are present in the tissue phantom at a depth of 15 and 45 mm and 4 cylinders of 10 mm diameter at depths of 70, 100, 130 and 160 mm. The background region is chosen to be a ring around the cyst with the same area as the region where the cyst statistics are calculated. This ensures that for the calculation of the statistics approximately the same amount of points are used for the cyst and background region. The edges of the cysts are excluded from the calculation so that changes in resolution do not affect the contrast [32]. Here we used 0.6 or 0.8 of the cyst diameter for the small and large cysts respectively as statistics region. To limit the effect of probe placement and the exact areas that are used to calculate the CNR, eleven measurements have been done on the same cysts and the calculated CNRs have been

averaged. Between the measurements the probe was shifted or rotated.

## IV. RESULTS

### A. Wire phantom

Fig. 3 shows the images obtained with the four methods using simulation data. The wires appear at the same position in each image, but the lateral width differs between the images. With DRF the largest lateral width is obtained, while PAM and PSASB 1 appear to obtain the smallest lateral width. There is however a distinct difference between PAM and PSASB 1. In the image of PSASB 1 artefacts appear around the point scatterers that become wider further away from the focus. The artefacts are at a level of about  $-35$  dB compared to the point scatterers. The artefacts vanish with PSASB 2, which in contrast to PSASB 1 applies a Hann window before summation. The remaining artefacts are at a level of  $-55$  dB or lower, which is 20 dB lower compared to the artefacts that appear in the image made with PSASB 1. The cost of the reduction in artefacts is a worse lateral resolution. With PAM the lateral resolution is as good as in the image obtained with PSASB 1, but without any extra artefacts as compared to PSASB 2. This indicates a clear advantage of using the wave equation over a time of flight approach as with the wave equation there is no trade-off between artefacts and resolution.

The differences between the methods as discussed before can also be observed in the measurement images visible in Fig. 4. The main difference with the simulated images is the appearance of extra artefacts. For example, there are reverberations visible below the wires. However, these extra artefacts appear in all measurement images and are therefore caused by the measurement setup and not by the different imaging methods.

The  $-6$  dB lateral PSF width of the previously discussed images is shown in Fig. 5. This figure also shows that the simulation and measurement results correspond very well to each other. Moreover, it is also visible that PAM and PSASB 1 obtain the best lateral resolution over the whole depth range. Compared to PSASB 2, the lateral width is on average 17% smaller while the difference with DRF is on average even 31%. Only around the transmit focus, the lateral resolution of each method is similar as expected.

PSASB and PAM obtain a lateral width that increases linearly with depth, which was also observed for PSASB by Bera *et al.* [8]. This indicates a constant angular resolution over depth. The theoretical far field lateral width calculated using the method described in Appendix A also shows a linearly increasing width. Furthermore, both PSASB 1 and PAM match the theoretical far field width. Because the theoretical width indicates a focus in transmit and receive, this shows that both PAM and PSASB 1 manage to completely focus the image at all depths.

The  $-20$  dB PSF width, which is not shown, has the same trend as the  $-6$  dB width. Around the transmit focus all methods perform similarly, but the best overall resolution is achieved by PSASB 1 and PAM.

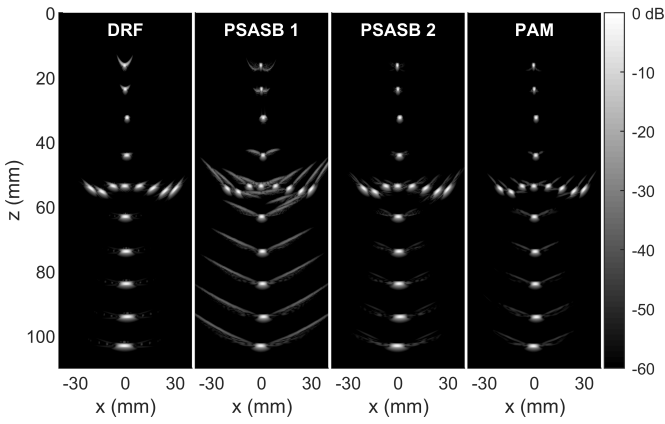


Fig. 3. Simulation results for the wire phantom. The scatterers in the simulation were positioned at equal positions as in the measurement for best comparison.

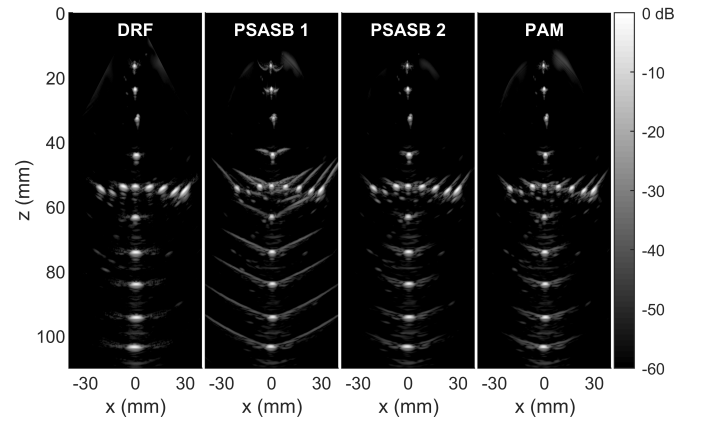


Fig. 4. Measurement results for the wire phantom.

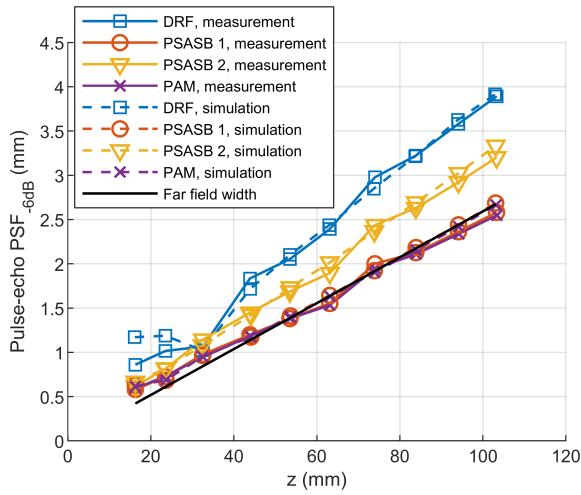


Fig. 5. The  $-6$  dB lateral width of the PSF for the wire phantom, corresponding to the images in Fig. 3 and 4

### B. Tissue phantom

Fig. 6 shows the result of the measurements on the tissue phantom. The different objects in the phantom are clearly visible in all the images, except for the deepest parts where noise starts to play a significant role. The artefacts that were visible in Fig. 3 and 4 for PSASB 1 are now hidden beneath the speckle pattern.

The obtained lateral resolution is again the narrowest with PAM and PSASB 1. This can for example be observed at the lower left cyst and at the resolution wires, which appear on the right side at a depth of 60 mm and 100 mm. The resolution is quantified in Fig. 7. On average the resolution obtained with PSASB 1 and PAM is 17% narrower than PSASB 2 and even 32% narrower than DRF, which is very similar to the values obtained in the wire phantom. For depths lower than approximately 120 mm the lateral resolution increases linearly with depth. Deep in the medium however the lateral resolution quickly deteriorates. There are two main causes. First of all, the signal-to-noise ratio in this area is low, which for example also results in the non-black appearing hypoechoic cyst in the

lower left of Fig. 6. Also, the attenuation lowers both the bandwidth and central frequency of the returned signal, and hence reduces the resolution.

### C. Contrast-to-Noise Ratio

The contrast-to-noise ratio is calculated from two cysts with a diameter of 6.7 mm and four cysts of 10 mm. A subset of the cysts is shown in Fig. 8, where the resulting image of one of the measurements used for calculating the CNR is shown together with the areas that are used to calculate the statistics of the cysts and background. The averaged CNR over all eleven measurements together with the standard error can be found in Fig. 9. The CNR obtained with each method decreases with depth. For the two smaller cysts there is hardly any distinction between DRF, PSASB 2 and PAM, but PSASB 1 performs slightly worse. This is most likely caused by the artefacts visible in Fig. 3 and 4. For the four deeper lying cysts, PSASB 1 continues to produce a systematically lower mean CNR compared to PSASB 2 and PAM due to these artefacts. Also for these four cysts, the mean CNR obtained with PAM is initially better, but the performance deteriorates with depth as compared to the other methods. It seems therefore that PAM suffers most from a low signal-to-noise ratio (SNR). The low SNR deep in the medium could be observed in Fig. 6.

### D. Variation of $f$ -number

Fig. 10 shows the lateral resolution that is obtained with PAM for different  $f$ -numbers in the first stage. For the smallest  $f$ -number the lateral resolution is worst, but for the larger  $f$ -numbers the width is always close to the theoretical far field width. While the opening angle decreases for increasing  $f$ -numbers, and therefore the number of contributing scan lines also decreases, the aperture of the virtual array at the focal depth increases. These effects cancel each other out and therefore the  $f$ -number has a limited effect on the lateral resolution. Only for very close focal distances this does not apply. The independence of the lateral resolution from the focal depth for large  $f$ -number can also be derived from (19)

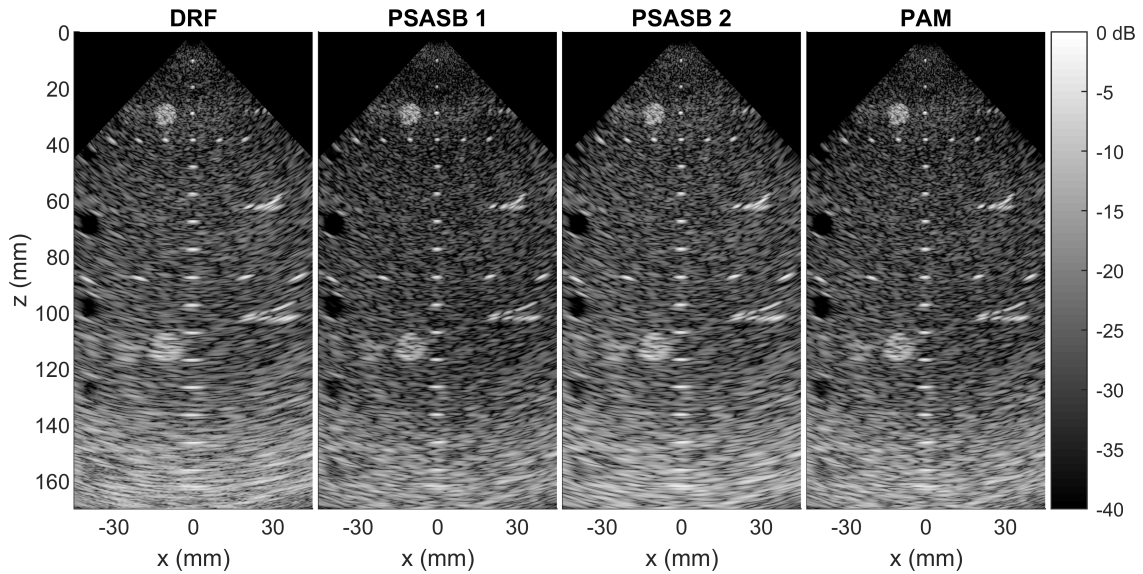


Fig. 6. Measurement results for the tissue phantom.

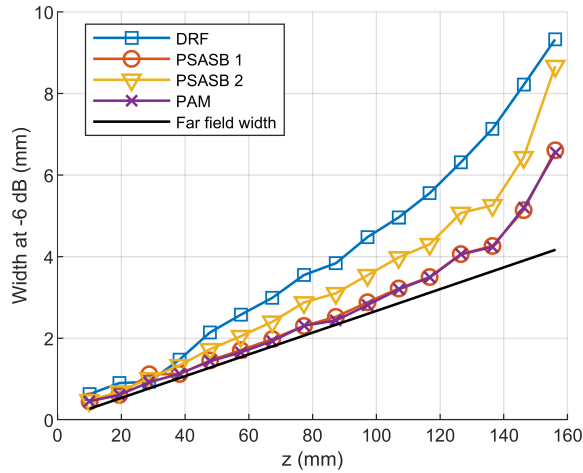


Fig. 7. The  $-6$  dB lateral width of the PSF for the tissue phantom, corresponding to the image in Fig. 6

and (21). For a large focal distance, the opening angle can be approximated using the first term of its Taylor series and this reduces (21) for an unsteered beam to

$$m_{\max}(f) = \frac{\pi f D}{\hat{c}}. \quad (24)$$

The above equation indicates that  $m_{\max}$ , and thus also the lateral resolution, becomes independent of the focal distance for large  $f$ -numbers.

For the current setup the results indicate that any  $f$ -number larger than 0.5 is sufficient to obtain the best possible resolution. This also applies to PSASB 1 and 2, which also show that the resolution is independent of  $f$ -numbers for large focal distances. The artefacts do however change for each two-stage method if the  $f$ -number changes. A focus near the probe result in more artefacts deep in the medium, while a deeper focus results in the opposite. Besides this, in setups where attenuation plays a significant role, the resolution deep in the

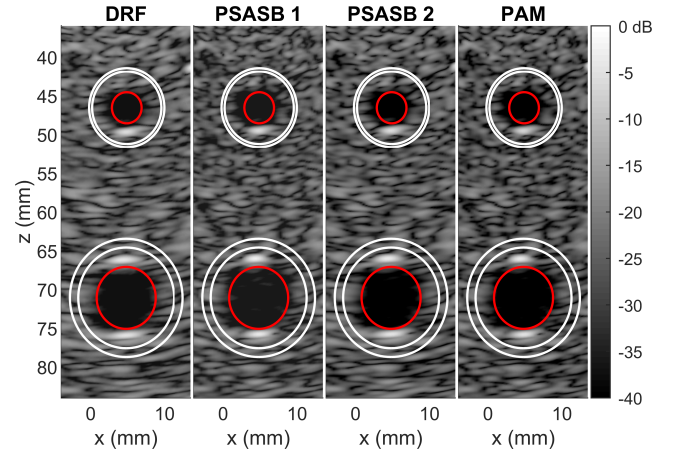


Fig. 8. The images obtained with one of the measurements that has been used to calculate the CNR. The area within the red line is used for calculating the cyst statistics, while the area between the white lines is used as background.

medium might deteriorate due to the low SNR as could be observed in Fig. 7. It might thus be necessary to tune the  $f$ -number for a specific situation, but the differences between DRF, PSASB and PAM do not disappear.

## V. DISCUSSION

In this paper we developed a computationally efficient two-stage beamforming method for phased arrays that reduces the required data flow using a simple front-end algorithm. In the second stage the scan data is further beamformed to obtain images that are synthetically focused over the entire image. Contrary to the time of flight approach in PSASB, we use a method based on the wave equation in the second stage.

The main advantage of Stolt migration for a linear array was the computation time reduction compared to SASB [13]. The computational efficiency of Stolt migration was achieved by a change of variables, after which all integrations could be evaluated using FFTs. For the method presented in this

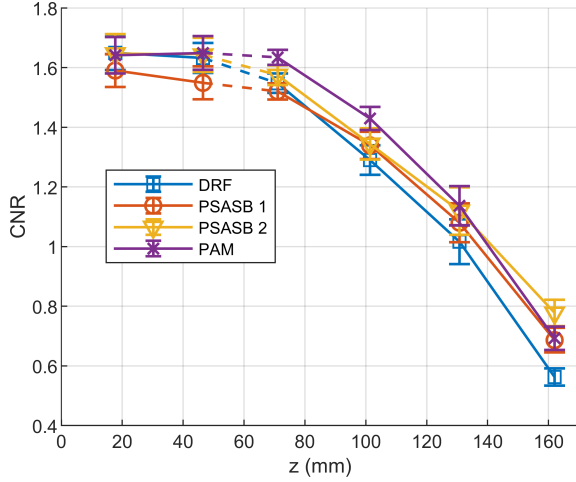


Fig. 9. Mean CNR together with the standard error from the measurements on the anechoic cysts in the CIRS Phantom. The two shallowest cysts have a diameter of 6.7 mm, while the deepest four have a diameter of 10 mm.

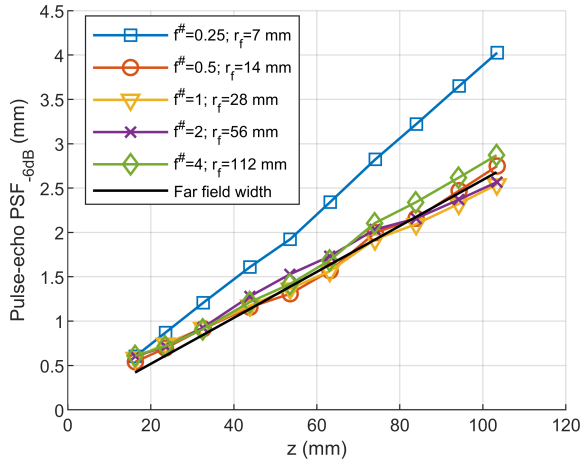


Fig. 10. The obtained resolution in the wire phantom for different first stage  $f$ -numbers.

paper we also applied a change of variables, after which the algorithm also could be done using Fourier Transforms. The required frequency domain interpolation was taken care of by the nonuniform Fourier Transform. In Table II a comparison is made between the number of operations required after pre-computation for PSASB, our migration algorithm which employs the FHT and the migration algorithm which calculates (14) using a matrix multiplication. Constant factors are neglected. In this table  $N_s$  is the number of depth samples,  $N_\theta$  is the number of angles,  $N_m$  is the number of angular frequencies,  $J$  is the number of neighbours used in the NUFFT and  $S$  is the upsampling factor. When inserting regular values of  $N_s = 1024$ ,  $N_\theta = 256$ ,  $N_m = 1024$ ,  $S = 4$  and  $J = 5$  the numbers in the rightmost column are obtained. First of all, it can be seen that using a NUFHT severely reduces the number of operations required compared to the matrix multiplication algorithm. The matrix multiplication scales with  $N_s^3$ , while the FHT approximately scales with  $N_s \log(N_s)$ . This reduces the total amount of operations by about four orders of magnitude.

The amount of memory required to store the pre-calculated

TABLE II  
THE AMOUNT OF OPERATIONS REQUIRED FOR THE DIFFERENT ALGORITHMS. FOR PAM THE AMOUNT REQUIRED FOR THE INDIVIDUAL STEPS IS ALSO SHOWN. THE FOLLOWING VALUES WERE USED  $N_s = 1024$ ,  $N_\theta = 256$ ,  $N_m = 1024$ ,  $S = 4$  AND  $J = 5$ .

Method	Operations	Amount
PSASB	$N_s N_\theta^2 S$	$2.68 \times 10^8$
PAM - FHT		$1.24 \times 10^8$
- 2D-FFT	$N_m N_s \log(N_m N_s)$	$2.10 \times 10^7$
- FHT		$9.23 \times 10^7$
* Division	$N_m N_s$	$1.05 \times 10^6$
* NUFFT	$N_m (N_s \log(N_s) + J N_s)$	$3.15 \times 10^7$
* Multiplication	$N_m S N_s$	$4.19 \times 10^6$
* NUFFT	$N_m (S N_s \log(S N_s) + J N_s)$	$5.56 \times 10^7$
- Inverse FFT	$N_s N_m \log(N_m)$	$1.05 \times 10^7$
PAM - Matrix multiplication		$1.10 \times 10^{12}$
- 2D-FFT	$N_m N_s \log(N_m N_s)$	$2.10 \times 10^7$
- Matrix multiplication	$N_m N_s^3$	$1.10 \times 10^{12}$
- Inverse FFT	$N_s N_m \log(N_m)$	$1.05 \times 10^7$

values is also significantly lower for the FHT method. In both cases order  $N_m$  different matrices containing the pre-calculated Hankel functions have to be stored, but these matrices contain  $N_s^2$  values in case of the matrix multiplication scheme is used and only  $N_s \times S$  in case of the FHT algorithm. This means that about 256 times less memory is required for the FHT algorithm.

This amount of operations required for the migration algorithm presented is very similar to the amount required for PSASB. This similarity was also observed in the computation time of the Matlab implementations of PSASB and our migration algorithm. The time on an Intel I5-6500 (Intel Corp., Santa Clara, California, USA) for both algorithms was about half a second, but these times are of course strongly related to the program efficiency and measurement setup. It should be noted that it is possible to start building the final image in (P)SASB while the data is still being captured, while for PAM the forward transform over the angles can only be done after all first stage lines are made. Still, we believe that for both algorithms real-time implementation should be achievable. The difference in amount of operations between PSASB and PAM is smaller than between SASB and Stolt migration [13]. This is mainly because after pre-computation 2 NUFFTs required to compute the Hankel transform, while in Stolt migration there was only a single FFT required for the same kind of operation.

In the NUFHT the exponential grid depends on the parameters  $f_0$ ,  $\alpha$  and  $r_0$ , as can be seen in (15), and the upsampling factor  $S$ . The exact choice of parameters depends on both the signal bandwidth and the imaging depth. In our situation, the parameters are mainly determined by the imaging depths and in this case the following choice of the other parameters can be used: The parameter  $r_0$  is set to the maximum imaging depth, while  $\alpha$  is set such that the complete radial grid encompasses all imaging depths. The minimum frequency  $f_0$  is then set such that the maximum frequency is twice the centre frequency. Finally, an upsampling factor of 4 is enough to prevent any visible artefacts.

The results that were obtained with the PAM match very

well with the theoretical limit for the  $-6$  dB PSF width, which represents focusing in both transmission and reception. This is visible in Fig. 5 and 7. This implies that the entire image is completely focused in transmit and receive. Therefore, a better resolution cannot be obtained using conventional imaging techniques.

The resolution obtained with PSASB 1 also matches the theoretical limit, but there are additional artefacts in the image. These artefacts appear because PSASB just uses a simple time of flight approach to calculate the delays for each contributing scanline before summation. In case there is a high amplitude scatterer present and nothing else, there is nothing preventing the scatterer to appear on every neighbouring image line. This is clearly visible in Fig. 3 and 4. In the tissue phantom these artefacts are not visible, but it does seem to result in a lower CNR. To prevent these artefacts, PSASB 2 weighs the scanlines before summation. This does however negatively affect the lateral resolution. PAM does not have this trade-off between artefacts and resolution. The wave equation does not only take into account the geometrical travel times of the wavefront, but it applies different complex weighing factors to all the wave components in the wavenumber-frequency domain. As a result, the field that is scattered by each point is approximated as close as physics allows. The effect of this is that the artefacts do not appear and that the lateral resolution is at the theoretical limit. This clearly shows the advantage of using the wave equation over a time-of-flight approach.

To account for the limited opening angle of the virtual sources/receivers we have employed a filter based on (20), which gives the highest expected angular frequency  $m$  for a certain frequency  $f$ . The filter mainly affected the CNR. Without the filter, the mean CNR obtained with PAM was lower at all cysts with the largest difference obtained at the deepest two cysts. Without the filter the mean CNR was equal to mean CNR obtained with DRF at these two cysts, which is worse than PSASB 1 and 2. In the images the effect of the filter was most easily observed in low SNR conditions. For example, deep in the tissue phantom a white noise pattern could be observed in the images without the filter. In the wire phantom no visible difference was observed with and without the filter. The lateral resolution was not affected at all, showing that the improvement in lateral resolution is not due to the applied filter.

Equation (18) gives a criterion for the angle between subsequent scanlines to avoid aliasing. This criterion shows that at least 205 scanlines within a  $90^\circ$  sector are required. In practice, some aliasing for the highest frequencies may be acceptable, especially when apodization is applied in transmit and receive. Apodization dampens the edges of the beamprofile, which give rise to the highest spatial frequencies in the angular direction. This corresponds to the effect that apodization leads to a broader PSF. It turns out that even with half the line density that was used for the images in this paper (i.e. 128 lines within a  $90^\circ$  sector), there were still no additional artefacts visible above  $-60$  dB in the experimental images (not shown) of the wire phantom and tissue phantom. This shows in this case that at least a 65% higher framerate is possible than follows from the criterion. Note that the discussion in this paragraph also

applies to PSASB.

In principle our algorithm could be extended from 2D to 3D, that is from a circular geometry to a cylindrical or spherical one. The derivation for the cylindrical geometry can for example be found in the paper by Skjelvareid *et al.* [17]. However, a large field-of-view without aliasing artefacts will result in a very low frame rate. This indicates that two stage beamforming methods using focused beams in 3D may not be suitable for real-time imaging.

## VI. CONCLUSION

In this paper we have developed a computationally efficient two stage beamforming method for phased arrays that is based on the wave equation. In the first stage a simple single focus DAS is used that reduces the amount of data from channel to scanline data. The second is based on the wave equation and is computationally efficient due to the application of the fast Hankel transform. Compared to PSASB in both simulations and measurements, our method requires a similar amount of operations to construct the image and does not have a trade-off between resolution and artefacts. These results show the advantage of using the wave equation in the second stage instead of a time of flight method in a two-stage approach.

## APPENDIX A

### THEORETICAL FAR FIELD BEAMWIDTH

The pressure generated by an array can be calculated using the Rayleigh-Sommerfeld integral. In the far field it turns out that the pressure as function of the angle  $\theta$  is proportional to [33, eq. 7.6, 7.9]

$$\hat{p}(\theta, f) \sim if\hat{v}(f) \operatorname{sinc}\left(\frac{fW \sin(\theta)}{c}\right) \sum_{m=1}^N a_m e^{im\Delta\phi} e^{\frac{2\pi ifx_m}{c} \sin\theta} \quad (25)$$

In this equation  $\hat{v}(f)$  is temporal Fourier transform of the normal velocity,  $W$  is the width of an element,  $a_m$  describes the apodization and  $\Delta\phi$  is the change in phase for successive elements. The constants of proportionality and the dependence on  $r$  have been neglected as we are interested in the beam profile only. To calculate the beam directivity for an arbitrary excitation pulse, first  $\hat{v}(f)$  is determined by taking the temporal Fourier transform of the pulse. Next, the above equation is evaluated for a dense grid of frequencies within the pulse bandwidth. After that, the calculated field is transformed back to the time domain and the maximum value of the envelope is taken as pressure amplitude. From the pressure amplitude the angular  $-3$  dB width can be determined, which is equal to the pulse-echo  $-6$  dB width. Finally, the angular width can be converted to the lateral width by using trigonometry.

## REFERENCES

- [1] J. Powers and F. Kremkau, "Medical ultrasound systems," *Interface focus*, vol. 1, no. 4, pp. 477–489, 2011.
- [2] B. Hope, "What's next for portable ultrasound?" 2012. [Online]. Available: <https://www.itnonline.com/article/what's-next-portable-ultrasound>

- [3] J. Kang, C. Yoon, J. Lee, S.-B. Kye, Y. Lee, J. H. Chang, G.-D. Kim, Y. Yoo, and T.-k. Song, "A system-on-chip solution for point-of-care ultrasound imaging systems: Architecture and ASIC implementation," *IEEE transactions on biomedical circuits and systems*, vol. 10, no. 2, pp. 412–423, 2016.
- [4] B. Lam, M. Price, and A. P. Chandrakasan, "An ASIC for Energy-Scalable, Low-Power Digital Ultrasound Beamforming," in *Signal Processing Systems (SiPS), 2016 IEEE International Workshop on*. IEEE, Year, Conference Proceedings, pp. 57–62.
- [5] C. Dusa, S. Kalalii, P. Rajalakshmi, and O. Rao, "Integrated 16-Channel Transmit and Receive Beamforming ASIC for Ultrasound Imaging," in *Proceedings of the IEEE International Conference on VLSI Design*, vol. 2015-February, no. February. IEEE, 2015, pp. 215–220.
- [6] C. Bradley, "Retrospective transmit beamformation," *Siemens Medical Solutions USA, Inc.*, 2008. [Online]. Available: [https://www.siemens.com.tr/i/Assets/saglik/Whitepaper\\_Bradley.pdf](https://www.siemens.com.tr/i/Assets/saglik/Whitepaper_Bradley.pdf)
- [7] J. Kortbek, J. A. Jensen, and K. L. Gammelmark, "Sequential beamforming for synthetic aperture imaging," *Ultrasonics*, vol. 53, no. 1, pp. 1–16, 2013.
- [8] D. Bera, J. G. Bosch, N. de Jong, and H. J. Vos, "Synthetic aperture sequential beamforming for phased array imaging," in *Ultrasonics Symposium (IUS), 2015 IEEE International*. IEEE, 2015, pp. 1–4.
- [9] M. C. Hemmsen, P. M. Hansen, T. Lange, J. M. Hansen, K. L. Hansen, M. B. Nielsen, and J. A. Jensen, "In vivo evaluation of synthetic aperture sequential beamforming," *Ultrasound in medicine & biology*, vol. 38, no. 4, pp. 708–716, 2012.
- [10] P. M. Hansen, M. Hemmsen, A. Brandt, J. Rasmussen, T. Lange, P. S. Krohn, L. Lönn, J. A. Jensen, and M. B. Nielsen, "Clinical evaluation of synthetic aperture sequential beamforming ultrasound in patients with liver tumors," *Ultrasound in medicine & biology*, vol. 40, no. 12, pp. 2805–2810, 2014.
- [11] M. C. Hemmsen, T. Kjeldsen, L. Lassen, C. Kjær, B. Tomov, J. Mosegaard, and J. A. Jensen, "Implementation of synthetic aperture imaging on a hand-held device," in *Ultrasonics Symposium (IUS), 2014 IEEE International*. IEEE, Year, Conference Proceedings, pp. 2177–2180.
- [12] M. C. Hemmsen, L. Lassen, T. Kjeldsen, J. Mosegaard, and J. A. Jensen, "Implementation of real-time duplex synthetic aperture ultrasonography," in *Ultrasonics Symposium (IUS), 2015 IEEE International*. IEEE, Year, Conference Proceedings, pp. 1–4.
- [13] H. J. Vos, P. L. van Neer, M. M. Mota, M. D. Verweij, A. F. van der Steen, and A. W. Volker, "F-k domain imaging for synthetic aperture sequential beamforming," *Ultrasonics, Ferroelectrics, and Frequency Control, IEEE Transactions on*, vol. 63, no. 1, pp. 60–71, 2016.
- [14] R. Stolt, "Migration by fourier transform," *Geophysics*, vol. 43, no. 1, pp. 23–48, 1978.
- [15] G. F. Margrave, "Numerical methods of exploration seismology with algorithms in matlab," *The University of Calgary Publ*, 2001, Available: <https://www.crewes.org/ResearchLinks/FreeSoftware/NumMeth.pdf>.
- [16] A. J. Hunter, B. W. Drinkwater, and P. D. Wilcox, "The wavenumber algorithm for full-matrix imaging using an ultrasonic array," *IEEE transactions on ultrasonics, ferroelectrics, and frequency control*, vol. 55, no. 11, pp. 2450–2462, 2008.
- [17] M. H. Skjeltvareid, Y. Birkelund, and Y. Larsen, "Synthetic aperture focusing of outwardly directed cylindrical ultrasound scans," *IEEE Transactions on Ultrasonics, Ferroelectrics, and Frequency Control*, vol. 59, no. 11, pp. 2460–2469, 2012.
- [18] C. H. Frazier and W. Brien, "Synthetic aperture techniques with a virtual source element," *Ultrasonics, Ferroelectrics, and Frequency Control, IEEE Transactions on*, vol. 45, no. 1, pp. 196–207, 1998.
- [19] P. Moon and D. E. Spencer, *Field theory handbook: including coordinate systems, differential equations and their solutions*. Springer, 2012.
- [20] M. Abramowitz and I. A. Stegun, *Handbook of mathematical functions: with formulas, graphs, and mathematical tables*. Dover Publications, Inc., 1972.
- [21] A. E. Siegman, "Quasi fast hankel transform," *Optics Letters*, vol. 1, no. 1, p. 13, 1977.
- [22] S. L. Marple, "Computing the discrete-time "analytic" signal via fft," *Ieee Transactions on Signal Processing*, vol. 47, no. 9, pp. 2600–2603, 1999.
- [23] Q. H. Liu and Z. Q. Zhang, "Nonuniform fast hankel transform (nufht) algorithm," *Applied Optics*, vol. 38, no. 32, p. 6705, 1999.
- [24] K. L. Peacock, "On the practical design of discrete velocity filters for seismic data processing," *Acoustics, Speech and Signal Processing, IEEE Transactions on*, vol. 30, no. 1, pp. 52–60, 1982.
- [25] R. Machiraju and R. Yagel, "Reconstruction error characterization and control: A sampling theory approach," *IEEE Transactions on Visualization and Computer Graphics*, vol. 2, no. 4, pp. 364–378, 1996.
- [26] J. A. Fessler and B. P. Sutton, "Nonuniform fast fourier transforms using min-max interpolation," *IEEE Transactions on Signal Processing*, vol. 51, no. 2, pp. 560–574, 2003.
- [27] P. Kruizinga, F. Mastik, N. de Jong, A. F. van der Steen, and G. van Soest, "Plane-wave ultrasound beamforming using a nonuniform fast fourier transform," *IEEE transactions on ultrasonics, ferroelectrics, and frequency control*, vol. 59, no. 12, pp. 2684–91, 2012.
- [28] B. P. Sutton, D. C. Noll, and J. A. Fessler, "Fast, iterative image reconstruction for mri in the presence of field inhomogeneities," *IEEE transactions on medical imaging*, vol. 22, no. 2, pp. 178–188, 2003.
- [29] J. A. Jensen and N. B. Svendsen, "Calculation of pressure fields from arbitrarily shaped, apodized, and excited ultrasound transducers," *IEEE Transactions on Ultrasonics, Ferroelectrics, and Frequency Control*, vol. 39.2, pp. 262–267, 1992.
- [30] J. A. Jensen, "Field: A program for simulating ultrasound systems," in *10th Nordic-Baltic Conference on Biomedical Engineering, Vol. 4, Supplement 1, Part 1: 351–353*. Citeseer, 1996, Conference Proceedings.
- [31] M. S. Patterson and F. S. Foster, "The Improvement and Quantitative Assessment of B-Mode Images Produced by an Annular Array/Cone Hybrid," *Ultrasonic Imaging*, vol. 5, no. 3, pp. 195–213, jul 1983.
- [32] O. M. H. Rindal, J. P. Åsen, S. Holm, and A. Austeng, "Understanding contrast improvements from capon beamforming," in *Ultrasonics Symposium (IUS), 2014 IEEE International*. IEEE, 2014, Conference Proceedings, pp. 1694–1697.
- [33] R. S. C. Cobbold, *Foundations of Biomedical Ultrasound*. Oxford University Press, 2007.